

On the operation of the chemo-thermal instability in primordial star-forming clouds

Thomas H. Greif^{1,2*}, Volker Springel^{3,4} and Volker Bromm⁵

¹ *Harvard-Smithsonian Center for Astrophysics, 60 Garden Street, Cambridge, MA 02138, USA*

² *Max-Planck-Institut für Astrophysik, Karl-Schwarzschild-Straße 1, 85740 Garching, Germany*

³ *Heidelberg Institute for Theoretical Studies, Schloss-Wolfsbrunnengasse 35, 69118 Heidelberg, Germany*

⁴ *Zentrum für Astronomie der Universität Heidelberg, Astronomisches Recheninstitut, Mönchhofstr. 12-14, 69120 Heidelberg, Germany*

⁵ *Department of Astronomy and Texas Cosmology Center, University of Texas, Austin, TX 78712, USA*

26 May 2022

ABSTRACT

We investigate the operation of the chemo-thermal instability in primordial star-forming clouds with a suite of three-dimensional, moving-mesh simulations. In line with previous studies, we find that the gas at the center of high-redshift minihaloes becomes chemo-thermally unstable as three-body reactions convert the atomic hydrogen into a fully molecular gas. The competition between the increasing rate at which the gas cools and the increasing optical depth to H₂ line emission creates a characteristic dip in the cooling time over the free-fall time on a scale of about 1000 au. As the effective equation of state drops from about 1.1 to well below unity, the free-fall time decreases to below the sound-crossing time, and density perturbations induced by transonic turbulence can grow. This allows the cloud to fragment on a scale of a few tens of au during the initial free-fall phase. In two of the nine haloes investigated, Jeans-unstable clumps condense out of the parent cloud, which will likely collapse before they are accreted by the primary clump. In the other haloes, fragmentation at such an early stage is less likely. However, given that previous simulations have shown that the infall velocity decreases substantially once the gas becomes rotationally supported, the amount of time available for perturbations to develop may be much greater than is evident from the limited period of time simulated here.

Key words: early Universe – cosmology: theory – galaxies: formation – galaxies: high-redshift – hydrodynamics – stars: formation

1 INTRODUCTION

The first stars in the Universe are believed to have formed only a few hundred million years after the Big Bang (Barkana & Loeb 2001; Bromm & Larson 2004; Ciardi & Ferrara 2005; Glover 2005; Loeb 2010; Glover 2013). They heated and ionised the pristine intergalactic medium (IGM; Bromm et al. 2001; Schaerer 2002; Alvarez et al. 2006; Abel et al. 2007; Johnson et al. 2007; Yoshida et al. 2007; Whalen et al. 2008; Greif et al. 2009), and their supernova explosions enriched the primordial gas with the first heavy elements (Heger et al. 2003; Umeda & Nomoto 2003; Wise & Abel 2008; Greif et al. 2010). They fundamentally altered the thermal and chemical state of the gas out of which the first galaxies formed, which in turn initiated the first self-sustaining cycle of star formation, feedback and chemical

enrichment (Thoul & Weinberg 1996; Mac Low & Ferrara 1999; Madau et al. 2001; Oh & Haiman 2002; Ricotti et al. 2002; Wada & Venkatesan 2003; Dijkstra et al. 2004; Read et al. 2006; Wise & Abel 2008; Greif et al. 2010). Understanding the formation and properties of the first stars is thus an important step towards a comprehensive picture of structure formation in the early Universe.

The first theoretical studies of Population III star formation date back to the late 1960's, in which molecular hydrogen was recognised as a coolant of low-mass gas clumps that condensed out of the expanding Universe at high redshift (Saslaw & Zipoy 1967; Peebles & Dicke 1968; Hirasawa 1969; Matsuda et al. 1969; Takeda et al. 1969). Subsequent studies used simplified one-zone models to account for the dynamics of collapsing gas clouds in the presence of radiative cooling (Yoneyama 1972; Hutchins 1976; Silk 1977, 1983; Carlberg 1981; Kashlinsky & Rees 1983; Palla et al. 1983; Carr et al. 1984; Couchman & Rees 1986; Uehara et al. 1996;

* E-mail: tgreif@cfa.harvard.edu

Tegmark et al. 1997), while the first one-dimensional calculations of the simultaneous collapse of dark matter (DM) and gas were carried out in the context of the cold dark matter (CDM) paradigm (Haiman et al. 1996; Omukai & Nishi 1998; Nakamura & Umemura 1999). Three-dimensional simulations of Population III star formation had to await improvements in numerical simulation techniques, and were not possible until the late 1990's (Abel et al. 1998, 2000, 2002; Bromm et al. 1999, 2002).

Based on these pioneering studies, a now widely accepted ‘standard model’ of Population III star formation has emerged. In this picture, the first bound structures capable of hosting star formation are considered to be DM ‘minihaloes’ with virial masses $M_{\text{vir}} \gtrsim 10^5 M_{\odot}$, which collapse at redshifts $z \gtrsim 20$. At the center of these haloes, molecular hydrogen forms due to the non-negligible free electron fraction left over after recombination. The ro-vibrational states of H_2 are excited by collisions with atomic hydrogen and helium, which decay radiatively and cool the gas. The minimum temperature of about 200 K is reached at a density of $\simeq 10^4 \text{ cm}^{-3}$, where the level populations of H_2 transition into local thermal equilibrium (LTE; Abel et al. 1998, 2002; Bromm et al. 1999, 2002). Shortly thereafter, the central gas cloud becomes Jeans-unstable and collapses in its own right.

At densities $n_{\text{H}} \gtrsim 10^8 \text{ cm}^{-3}$, where n_{H} is the number density of hydrogen nuclei, three-body reactions convert the remaining atomic hydrogen into H_2 (Abel et al. 2002; Bromm & Loeb 2004; Yoshida et al. 2006; Turk et al. 2009). During this phase, the gas may become chemo-thermally unstable, since the rapidly increasing H_2 fraction results in increased cooling, which further accelerates the collapse and the rate at which H_2 is formed (Sabano & Yoshii 1977; Silk 1983; Omukai & Yoshii 2003). This runaway process is counteracted by the release of the binding energy of the formed H_2 , and the increasing optical depth of the gas to H_2 line emission. As the molecular hydrogen fraction saturates, collision-induced emission becomes important, followed by collisional dissociation of H_2 (Ripamonti & Abel 2004). The final, nearly adiabatic contraction of the cloud ends with the formation of a protostar with a mass of $\simeq 0.01 M_{\odot}$ (Omukai & Nishi 1998; Yoshida et al. 2008).

An inherent problem of self-gravitating collapse simulations is the continually decreasing timescale on which the gas evolves, which limits the integration time to of order a few dynamical times of the Jeans-unstable cloud. This problem may be circumvented by employing so-called sink particles, but comes at the cost of introducing artificial boundary conditions (Bate et al. 1995; Krumholz et al. 2004; Jappsen et al. 2005; Federrath et al. 2010). Recent studies that employed sink particles found that the gas becomes rotationally supported in a Keplerian disc. The disc becomes gravitationally unstable due to the high mass accretion rate from the envelope onto the disc and the efficient cooling of the disc by H_2 line emission, and fragments into a handful of protostars (Clark et al. 2008, 2011a, b; Stacy et al. 2010). A follow-up study that investigated a sample of minihaloes found that the star-forming clouds in them fragmented in a similar fashion (Greif et al. 2011).

Simulations that avoid sink particles and instead directly resolve the collapse of the gas to protostellar densities have become possible, but their high computational limits the integration time to $\sim 10 \text{ yr}$ (Greif et al. 2012). In analogy

to previous simulations with sink particles, this study finds that the circumstellar disc fragments into a small system of protostars. Strong torques exerted by the protostars and the disc result in the migration of about half of the protostars to the center of the cloud in a free-fall time, where they merge with the primary protostar. A smaller fraction of the protostars migrates to higher orbits and survives until the end of the simulation. Two-dimensional simulations with a piecewise polytropic equation of state show similar patterns of migration and merging (Vorobyov et al. 2013).

The susceptibility of the gas to fragmentation is a key ingredient towards understanding the initial mass function of the first stars. An early termination of fragmentation may result in the formation of a single, massive Population III star, while continued fragmentation may lead to the formation of a rich cluster of less massive stars. Most of the mass that is accreted before the gas is dispersed by ionising radiation resides between 10 and 1000 au (Tan & McKee 2004; McKee & Tan 2008; Hosokawa et al. 2011; Stacy et al. 2012), implying that it is crucial to understand the thermal evolution of the gas on these scales. In the present study, we use a suite of three-dimensional, moving mesh simulations to investigate the collapse of the gas on these scales in detail. Compared to previous work, we employ higher resolution and investigate a larger sample of haloes. This allows us to assess the properties of primordial gas clouds with unprecedented accuracy. In addition, we perform the most comprehensive resolution study of primordial star formation to date, using up to three billion resolution elements.

The structure of our work is as follows. In Section 2, we describe the numerical methodology, the setup of the simulations, and the chemistry and cooling network. In Section 3, we present the results of a one-zone calculation that highlights the various physical processes that operate on the relevant scales, discuss the thermal and gravitational stability of the gas in a representative halo in the three-dimensional simulations, followed by an analysis of the star-forming clouds in all haloes. We then discuss the results of the resolution study, and in Section 4 summarise our main findings and draw conclusions. All distances are quoted in proper units, unless noted otherwise.

2 SIMULATIONS

The three-dimensional, cosmological hydrodynamics equations for a mixed fluid consisting of collisionless DM and collisional gas are solved using the methodology employed in the moving-mesh code AREPO (Springel 2010). In the following, we describe in detail the initialisation and setup of the simulations.

2.1 Dark matter simulations

The background Universe used to initialise the simulations is a standard Λ cold dark matter (Λ CDM) cosmology with parameters based on the *WMAP* observations (e.g. Komatsu et al. 2009). We use a matter density of $\Omega_{\text{m}} = 1 - \Omega_{\Lambda} = 0.27$, baryon density $\Omega_{\text{b}} = 0.046$, Hubble parameter $h = 0.7$, spectral index $n_{\text{s}} = 0.96$, and normalisation $\sigma_8 = 0.81$. The matter power spectrum is evolved forward in time until $z = 99$, and we use the Zel’dovich approximation to determine the

initial displacements of the particles that represent the DM distribution function from a cubical lattice. We initialise nine boxes with a side length of 1 Mpc (comoving) and differing realisations of the power spectrum to investigate how our results are affected by cosmic variance. We employ 512^3 particles of mass $\simeq 272 M_\odot$, and use a gravitational softening length of $\simeq 98$ pc (comoving), which corresponds to 5% of the initial mean inter-particle separation. The simulations are evolved until the first halo grows to a virial mass of $M_{\text{vir}} = 5 \times 10^5 M_\odot$, which is evaluated by an on-the-fly friends-of-friends algorithm (Springel et al. 2001).

2.2 Resimulations

Once the halo designated for further refinement has been located, the simulations are centred on this halo and reinitialised with higher resolution. For this purpose the particles in the target halo and a sufficiently large boundary region around it are traced back to their initial positions, which yields the Lagrangian volume out of which the halo formed. In this region, the resolution is increased by a factor of 16^3 with respect to the original simulation, and augmented with additional small-scale power. Each DM particle is replaced by a less massive DM particle and gas cell with a displacement corresponding to half of the initial mean inter-particle separation, and a mass ratio of $M_{\text{gas}}/M_{\text{dm}} = \Omega_b/(\Omega_m - \Omega_b)$. Outside of the target region, the resolution is gradually decreased to reduce the total number of resolution elements, while the accuracy of the gravitational tidal field that influences the formation of the halo is preserved. The DM particle and gas cell masses in the high-resolution region are $\simeq 0.05$ and $\simeq 0.01 M_\odot$, respectively, corresponding to nearly 100 times higher resolution compared to Greif et al. (2011, 2012). The gravitational softening length is set to $\simeq 6$ pc (comoving).

The cosmological resimulations are run until the minimum cell size is of order 10^{-8} of the side length of the box. In the present version of AREPO, the number of exact integer operations used to construct a valid Voronoi tessellation increases substantially when the dynamic range exceeds the above value, which decreases the performance of the code. Nearly simultaneously, the maximum resolution of the Peano-Hilbert curve is reached and the cells can no longer be distributed efficiently among tasks. Both of these limitations will be addressed in a future version of the code. Here, we resort to extracting the central 1 kpc (comoving) of the box and reinitialising the simulations at the final output time. Once the density exceeds $n_{\text{H}} = 10^9 \text{ cm}^{-3}$, we perform a second extraction and cut out the central 1 pc, discard the DM particles, and evolve the simulations to a density of $n_{\text{H}} = 10^{15} \text{ cm}^{-3}$. The intermediate resimulations are necessary to achieve a maximum dynamic range in the final resimulations, which simplifies the analysis of the data. In both cases, the sound crossing time through the box is much longer than the free-fall time of the dense gas at the center, such that perturbations from the edge of the box do not affect the central cloud.

In terms of computational efficiency, AREPO has been further improved with respect to the version employed in Greif et al. (2012). One of the most important new features is a domain decomposition optimised for simulations with a high dynamic range, which allows close to optimal work bal-

Table 1. Halo properties

Simulation	z_{coll}	M_{vir} [$10^5 M_\odot$]	r_{vir} [pc]	λ
MH1	23.9	6.2	109	0.0094
MH2	19.2	14.0	176	0.056
MH3	20.1	15.5	175	0.019
MH4	24.1	4.4	97	0.031
MH5	22.4	5.1	109	0.0086
MH6	24.0	3.5	90	0.053
MH7	24.5	5.5	103	0.028
MH8	19.2	6.3	135	0.050
MH9	25.0	3.1	83	0.031

Redshift of collapse, virial mass, virial radius and spin parameter of the first minihaloes that form in the simulations.

ancing by taking into account the wall clock time spent on the various levels in the time step hierarchy. Furthermore, the gravitational oct-tree is now reconstructed at each time step, which prevents a dramatic increase in the wall clock time spent on the tree walk when the sizes of the nodes are adjusted dynamically to encompass all particles that are assigned to them. Finally, a separate neighbour tree is constructed to speed up the neighbour search used in particular for the construction of the Voronoi tessellation.

2.3 Refinement

The so-called Truelove criterion states that at least four cells per Jeans length are necessary to resolve gravitational instability (Truelove et al. 1998). However, this is generally not sufficient to resolve the turbulent cascade that is driven by gravitational collapse. For example, Federrath et al. (2011) showed that at least 32 cells per Jeans length are necessary to model the amplification of magnetic fields by the turbulent dynamo. In Turk et al. (2012), it was shown that the employed resolution affects the chemical, thermal and dynamical evolution of primordial gas clouds. In particular, the amount of rotational support increases as the resolution is decreased, which might affect the ability of the gas to fragment. Although the resolution requirements in a fixed grid simulation may not be the same as in a moving-mesh simulation, these results show that it is desirable to use as many cells per Jeans length as possible.

Turk et al. (2010) further found that it is advantageous to evaluate the Jeans length using the minimum temperature of the gas, which ensures that shock-heated regions are equally well resolved as cold regions. To facilitate a comparison with previous studies, we therefore also employ the refinement criterion proposed by Turk et al. (2010), and evaluate the Jeans length at $T_{\text{min}} = 200$ K, which yields:

$$\lambda_{\text{J}} \simeq 0.6 \text{ pc} \left(\frac{n_{\text{H}}}{10^4 \text{ cm}^{-3}} \right)^{-1/2}. \quad (1)$$

Using this definition, we refine cells if $h > \lambda_{\text{J}}/N_{\text{J}}$, where $h = (3V/4\pi)^{1/3}$ is the approximate radius of a cell, V its volume, and N_{J} the desired number of cells per Jeans length. For $N_{\text{J}} = 32$ and $n_{\text{H}} \gtrsim 10^8 \text{ cm}^{-3}$, the Jeans mass is resolved by $\simeq 10$ times more cells compared to Greif et al. (2012). In Section 3.3, we present a resolution study in which we systematically increase N_{J} from 8 to 128. Due to the excessive

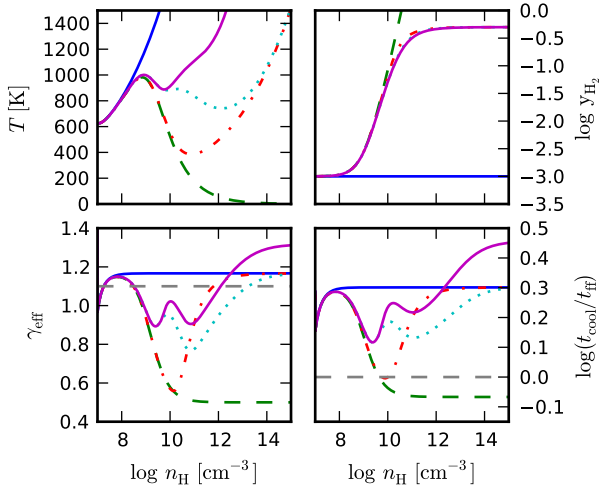


Figure 1. From top left to bottom right: temperature, H_2 fraction, effective equation of state, and cooling time over free-fall time versus number density of hydrogen nuclei in a one-zone calculation. The various profiles show the evolution for a constant H_2 fraction (blue), indefinitely increasing H_2 fraction (green), limited H_2 fraction (red), three-body formation heating (cyan), and an increasing optical depth to line emission (magenta). The dashed grey lines denote an effective equation of state of 1.1 and a cooling time equal to the free-fall time. If the H_2 fraction is allowed to increase indefinitely, the chemo-thermal instability results in an asymptotic $\gamma_{\text{eff}} = 1/2$. However, the decreasing H_2 fraction, three-body formation heating, and the optical depth of the gas reduce the effectiveness of the instability, such that the cooling time over the free-fall time drops only slightly below the value expected for a constant H_2 fraction.

computational cost of simulations with $N_J = 128$, we use 64 cells per Jeans length for the main simulation runs discussed in Sections 3.1 and 3.2.

In addition to the refinement based on the Jeans length, we refine cells if their mass increases to more than twice their initial mass. While AREPO maintains near constant mass resolution by advecting the cells in a Lagrangian fashion, the Eulerian mass flux between cells may lead to a gradual drift away from the initial masses of the cells.

2.4 Chemistry and cooling

The chemistry and cooling network employed in the present study is nearly identical to the one described in Greif et al. (2012). The species evolved next to the internal energy of the gas are H , H^+ , H^- , H_2^+ , H_2 , He , He^+ , He^{++} , D , D^+ , HD , and free electrons (Glover & Jappsen 2007; Clark et al. 2011). We use the publicly available SUNDIALS CVODE package to solve the coupled chemical and thermal rate equations (Hindmarsh et al. 2005). The abundances are computed with a relative accuracy of 0.1%, which is necessary for an accurate integration at high densities, where three-body reactions become important. The minimum abundance that is computed reliably is $y_X = 10^{-20}$, where y_X denotes the number density of species X with respect to the number density of hydrogen nuclei. This threshold prevents the solver from computing accurate abundances when it is not necessary.

The most important low-temperature coolant in pri-

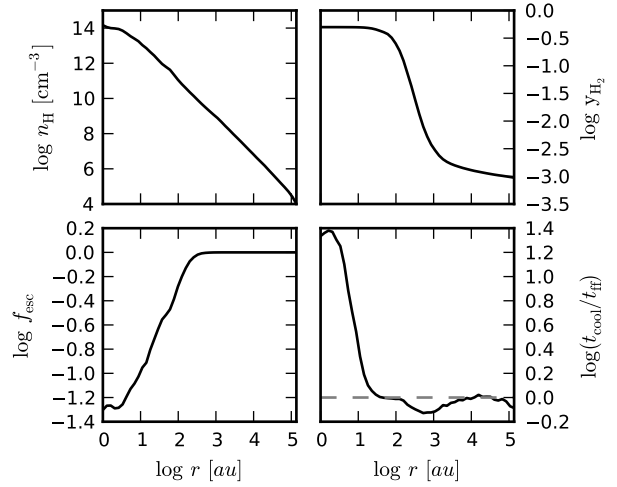


Figure 2. From top left to bottom right: number density of hydrogen nuclei, H_2 fraction, photon escape fraction, and cooling time over free-fall time versus radius. The dashed grey line denotes a cooling time equal to the free-fall time. The H_2 fraction rapidly increases below $\simeq 1000 \text{ au}$ due to three-body reactions, which results in the cooling time falling slightly below the free-fall time. As the optical depth of the gas to H_2 line emission increases, the cooling rate decreases again, and the cooling time remains nearly equal to the free-fall time down to scales of a few tens of au.

mordial gas is molecular hydrogen, which forms via associative detachment of H and H^- , following radiative association of H and e^- (Saslaw & Zipoy 1967; Abel et al. 1997; Galli & Palla 1998). The ro-vibrational states of H_2 are collisionally excited and decay radiatively, allowing the gas to cool to a minimum temperature of $T \simeq 200 \text{ K}$. At low densities, we use the excitation rates for collisions with neutral hydrogen atoms given by Wrathmall & Flower (2007), assuming an ortho-para ratio of 3:1. At high densities, when the energy states are populated according to LTE, we use the rates given by Le Bourlot et al. (1999). We neglect collisions with electrons, protons, and neutral helium atoms, which may provide a non-negligible amount of cooling at the relevant densities and temperatures (Glover & Abel 2008).

Another low-temperature coolant in primordial gas is hydrogen deuteride (HD), which may become important at temperatures $T \lesssim 200 \text{ K}$ due to its permanent dipole moment (Stancil et al. 1998; Flower et al. 2000; Nakamura & Umemura 2002; Johnson & Bromm 2006; Ripamonti 2007; McGreer & Bryan 2008; Greif et al. 2011). In minihalos, HD forms mainly via associative detachment of H_2 and D^+ , where the abundance of D^+ is set mainly by recombinations and charge transfer with H . The cooling rate of the gas by HD ro-vibrational transitions is given by Lipovka et al. (2005).

At densities $n_{\text{H}} \gtrsim 10^8 \text{ cm}^{-3}$, molecular hydrogen forms via three-body reactions, which heats the gas due to the release of the molecular binding energy (Palla et al. 1983; Bromm et al. 1999; Abel et al. 2002; Bromm et al. 2002; Yoshida et al. 2006). The corresponding reaction rates are highly uncertain, which is reflected by the substantial variation of the properties of primordial gas clouds when the different rates are used (Turk et al. 2011). We here adopt the

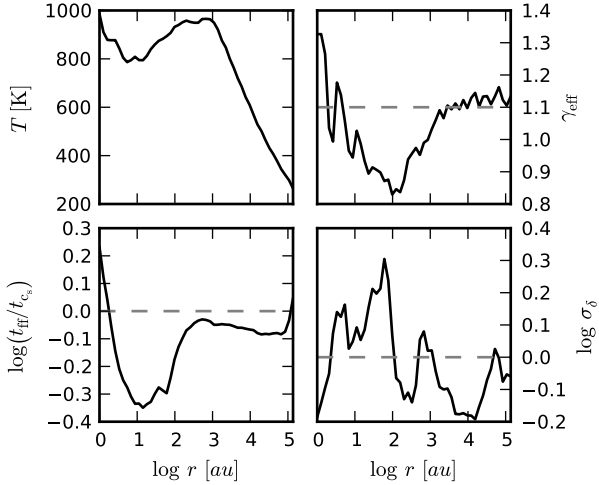


Figure 3. From top left to bottom right: temperature, effective equation of state, free-fall time over sound-crossing time, and RMS density contrast versus radius. The dashed grey lines denote an effective equation of state of 1.1, a free-fall time equal to the sound-crossing time, and an RMS density contrast of unity. As the cooling time decreases, the effective equation of state of the gas drops from $\gamma_{\text{eff}} \gtrsim 1.1$ to $\simeq 0.8$, resulting in a slight drop in temperature from $\simeq 1000$ K to $\simeq 800$ K below $\simeq 1000$ au. As a result, the free-fall time falls below the sound-crossing time and perturbations seeded by the transonic turbulence within the cloud can grow. This is evident from the bottom right panel, which shows that the RMS density contrast increases from about $\sigma_\delta \simeq 0.6$ on a scale of $\simeq 10^4$ au to well above unity on a scale of $\simeq 100$ au.

intermediate rate for three-body H_2 formation among those of Turk et al. (2011), which is taken from Palla et al. (1983). For $n_{\text{H}} \gtrsim 10^{10} \text{ cm}^{-3}$, column densities are high enough that the gas becomes optically thick to H_2 line emission, and we use the Sobolev approximation to determine the escape fraction of photons emitted by H_2 lines (Yoshida et al. 2006).

In contrast to Greif et al. (2012), we do not switch to an equilibrium chemistry solver at a density of $n_{\text{H}} = 10^{14} \text{ cm}^{-3}$, since we only follow the collapse up to a density of $n_{\text{H}} = 10^{15} \text{ cm}^{-3}$. However, we include a number of performance optimisations that decrease the computational cost of the non-equilibrium solver by a factor of a few. In particular, we improve cache utilisation by minimising the time spent on the retrieval of reaction rates, which are accessed repeatedly as the abundances are evolved. Finally, our main simulations do not include species transfer between cells, which has only recently been implemented in AREPO. However, we have performed a test simulation in which we follow the high-density evolution of the gas in MH1 using species transfer, and found that it only marginally affects our results.

2.5 Analysis

The number of resolution elements employed in the main simulations exceeds 10^9 , which is an increase by more than two orders of magnitude compared to the simulations presented in Greif et al. (2011, 2012). Such large datasets also require more sophisticated tools for an efficient analysis. To this end, we have written the parallel software package SATOR, which uses the message passing interface (MPI) to

read datasets in C and distribute the particle load to the processing cores. The operations required for the various tasks, e.g. the image generation or the computation of radial profiles, are then performed on the particles residing on each core, allowing near-optimal work balance. Upon completion, an intermediate dataset is written that is pipelined to a Python program for further analysis. The combined workflow of SATOR is controlled by a script that reads in a minimal set of parameters from the command line, which specifies the mode of operation and the target dataset. The script may be run interactively, or submitted to a queuing system for very large datasets and time-consuming calculations. On a Sandy bridge computing cluster, the runtime of SATOR to analyze our largest dataset with $\simeq 3 \times 10^9$ cells using 512 MPI tasks is of order 10 s, which is a substantial improvement compared to Greif et al. (2011, 2012).

3 RESULTS

3.1 Chemo-thermal instability

3.1.1 One-zone model

To qualitatively understand the influence of the various physical processes on the relevant scales, we perform a one-zone collapse calculation that employs a simplified chemistry and cooling model. In a roughly isothermally contracting cloud, the rate at which the core density increases is given by:

$$\dot{n}_{\text{H}} = n_{\text{H}}/t_{\text{ff}}, \quad (2)$$

where $t_{\text{ff}} = \sqrt{3\pi/(32G\rho)}$, G is Newton’s constant, $\rho = m_{\text{H}}n_{\text{H}}/X$ is the mass density, m_{H} is the mass of the hydrogen atom, and $X = 3/4$ is the cosmological mass fraction of hydrogen. The volumetric heating rate of the gas in $\text{erg s}^{-1} \text{ cm}^{-3}$ is given by:

$$\dot{u} = \gamma u/t_{\text{ff}} - Ay_{\text{H}_2}f_{\text{esc}}\left(\frac{n_{\text{H}}}{\text{cm}^{-3}}\right)\left(\frac{T}{\text{K}}\right)^\alpha + Bn_{\text{H}}\dot{y}_{\text{H}_2}, \quad (3)$$

where γ is the adiabatic index of the gas, y_{H_2} the molecular hydrogen fraction, $A = 10^{-33} \text{ erg cm}^{-3} \text{ s}^{-1}$ and $\alpha = 4$ approximate the H_2 line cooling function used in the full three-dimensional simulations, $B = 4.48 \text{ eV}$ is the binding energy of the H_2 molecule, and f_{esc} the photon escape fraction for H_2 line emission. The first term on the right-hand side of the equation describes adiabatic heating, the second term H_2 line emission, and the third term three-body formation heating. We have verified that all other thermal processes are comparatively sub-dominant at the relevant densities and temperatures. We use an adiabatic index of $\gamma = 5/3$ for a monatomic gas, even though the gas consists of a mix of atomic and molecular hydrogen. We also neglect the change in the mean molecular weight μ , which counteracts the effect of the varying γ in the relation between the energy density and temperature. The net effect of neglecting both processes is thus small. The photon escape fraction is given by:

$$f_{\text{esc}} = 1.45 \frac{x}{x^{1.45} + 0.45} \quad (4)$$

for $x \geq 1$ and $f_{\text{esc}} = 1$ for $x < 1$, where $x = n_{\text{H}}/n_{\text{H,thresh}}$ and $n_{\text{H,thresh}} = 4 \times 10^9 \text{ cm}^{-3}$. This formula is based on the

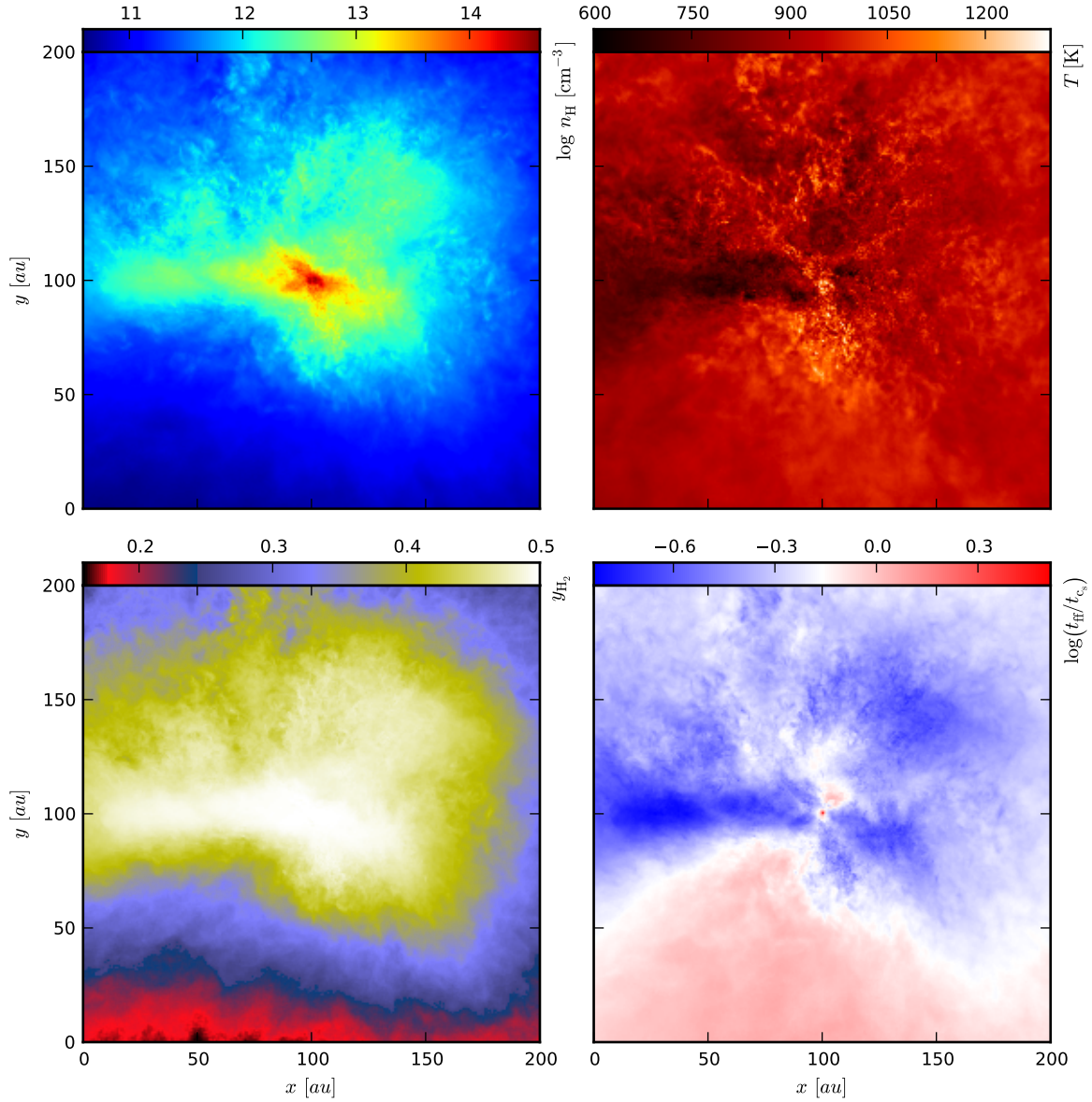


Figure 4. From top left to bottom right: number density of hydrogen nuclei, temperature, H_2 fraction, and free-fall time over sound-crossing time in a cube of side length 200 au, weighted with the mass and the square of the density of the cells traversed along the line of sight. As the chemo-thermal instability develops and the cooling time falls below the free-fall time, a secondary clump condenses out of the parent cloud that is visible on the left-hand side of the panels. The gravitational instability of the clump is evident from the bottom right panel, which shows that the free-fall time has dropped to well below the sound-crossing time.

fit provided by Ripamonti & Abel (2004), but has the advantage of a continuous derivative at $x = 1$. Finally, the rate at which H_2 molecules are formed is given by

$$\dot{y}_{\text{H}_2} = C (1 - 2y_{\text{H}_2})^3 \left(\frac{n_{\text{H}}}{\text{cm}^{-3}} \right)^2 \left(\frac{T}{\text{K}} \right)^{-1}, \quad (5)$$

where $C = 5.5 \times 10^{-29} \text{ s}^{-1}$. We have again verified that all other rate equations that affect the chemical composition of the gas are comparatively small at the relevant densities and temperatures. We initialise the calculations at a density of $n_{\text{H}} = 10^7 \text{ cm}^{-3}$, using a temperature of $T = 580 \text{ K}$ and an H_2 fraction of $y_{\text{H}_2} = 10^{-3}$. These initial conditions roughly correspond to the expected values at the initial density, and in

addition yield a smooth transition into the regime at which the chemo-thermal instability operates.

In Figure 1, we show the results of the one-zone calculation as we systematically increase the level of physical detail. The blue line shows the evolution for a constant H_2 fraction and a constant escape fraction of unity. In this case, the effective equation of state remains close to $\gamma_{\text{eff}} = 7/6$, since $t_{\text{cool}} \simeq t_{\text{ff}}$, which yields $T^{-3} \propto n_{\text{H}}^{-1/2}$ and thus $T \propto \rho^{1/6}$. The green line shows the collapse assuming that the H_2 fraction may increase indefinitely, the three-body formation rate is independent of the H_2 fraction, and that three-body formation heating as well as the influence of the decreasing es-

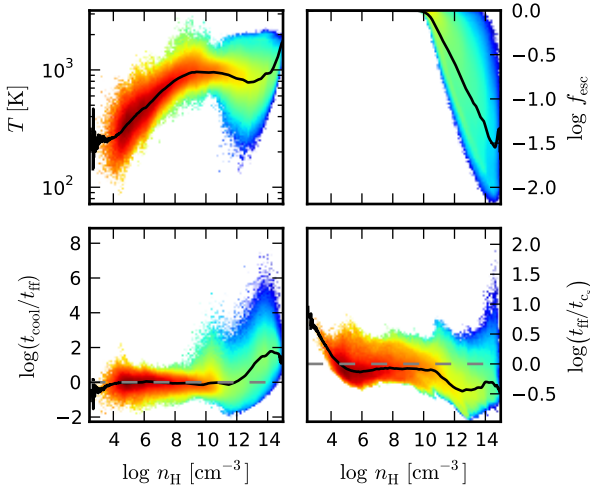


Figure 5. From top left to bottom right: temperature, escape fraction, cooling time over free-fall time, and free-fall time over sound-crossing time versus number density of hydrogen nuclei. The logarithm of the mass per bin over the total mass in the box is color-coded from blue (lowest) to red (highest), and the solid lines show the mass-weighted average value versus density. The grey dashed lines denote a cooling time equal to the free-fall time, and a free-fall time equal to the sound-crossing time. The temperature distribution widens significantly above $n_{\text{H}} \simeq 10^{10} \text{ cm}^{-3}$ as the cooling time falls below the free-fall time. The photon escape fraction at a given density fluctuates by up to two orders of magnitude, such that some regions of the cloud cool very efficiently and may become Jeans-unstable. This is reflected by the substantial amounts of gas with a free-fall time below the sound-crossing time.

cape fraction may be neglected. In this case, an asymptotic $\gamma_{\text{eff}} = 1/2$ is reached, which is evident from the following calculation.

The cooling time due to H_2 line emission in the optically thin limit is given by:

$$t_{\text{cool}} \propto y_{\text{H}_2}^{-1} T^{-3}, \quad (6)$$

and the derivative of the H_2 fraction with respect to n_{H} is given by:

$$\frac{dy_{\text{H}_2}}{dn_{\text{H}}} = \frac{dy_{\text{H}_2}}{dt} \frac{dt}{dn_{\text{H}}} \propto n_{\text{H}_2}^{3/2-\gamma_{\text{eff}}}, \quad (7)$$

where we have assumed $T \propto \rho^{\gamma_{\text{eff}}-1}$. Integration over n_{H_2} and insertion into equation (6) yields:

$$t_{\text{cool}} \propto n_{\text{H}_2}^{3/2-2\gamma_{\text{eff}}}, \quad (8)$$

and the cooling time over the free-fall time is thus given by:

$$\frac{t_{\text{cool}}}{t_{\text{ff}}} \propto n_{\text{H}_2}^{1-2\gamma_{\text{eff}}}. \quad (9)$$

A constant ratio of the cooling time to the free-fall time is therefore only possible for $\gamma_{\text{eff}} = 1/2$, which agrees with the results shown in Figure 1.

Under more realistic circumstances, this asymptotic value is never achieved, since only a finite amount of H_2 may be formed. In addition, the rate at which H_2 forms decreases as the H_2 abundance increases. The red line in Figure 1 denotes the case in which these considerations have been taken into account. As expected, the effective equation

of state departs from the asymptotic $\gamma_{\text{eff}} = 0.5$ as the H_2 abundance increases to of order unity, and quickly returns to $\gamma_{\text{eff}} = 7/6$. When three-body formation heating and the increasing optical depth to H_2 line emission are taken into account (cyan and magenta lines, respectively), the effectiveness of the chemo-thermal instability is further reduced, and the temperature, effective equation of state, and ratio of the cooling time to the free-fall time are significantly less affected. Nevertheless, an unstable regime develops at a density of $\gtrsim n_{\text{H}} \simeq 10^9 \text{ cm}^{-3}$, where γ_{eff} drops to $\simeq 0.9$.

3.1.2 Simulations

The properties of the gas in the three-dimensional simulations are similar, but not entirely equal to those of the one-zone calculations. In Figure 2, we show the number density of hydrogen nuclei, H_2 fraction, photon escape fraction, and cooling time over free-fall time versus radius r at the last output time of the high-density simulations in MH1. The profiles are determined by using a mass-weighted average of the cells that contribute to the radial bins. The top right panel shows that the H_2 fraction increases rapidly on a scale of $\simeq 1000 \text{ au}$ as three-body reactions become important. This results in the cooling time decreasing to about half of the free-fall time, which is evident from the dip at $r \simeq 1000 \text{ au}$. On a scale of $\simeq 500 \text{ au}$, the optical depth of the gas to H_2 line emission increases, and the cooling time again approaches the free-fall time.

In Figure 3, we show the temperature, effective equation of state, free-fall time over sound-crossing time, and root-mean-square (RMS) density contrast versus radius. The latter is given by:

$$\sigma_{\delta} = \sqrt{\sum_i \frac{m_i}{M_{\text{tot}}} \left(\frac{\rho_i - \bar{\rho}}{\bar{\rho}} \right)^2} \quad (10)$$

where the sum extends over all cells contributing to a radial bin, i denotes the cell under consideration, m_i its mass, ρ_i its density, M_{tot} the total mass per bin, and $\bar{\rho}$ the mass-weighted average density of the bin. Following the decrease of the cooling time below the free-fall time, the top left panel in Figure 3 shows that the temperature of the gas briefly decreases from $\simeq 1000 \text{ K}$ to $\simeq 800 \text{ K}$, which is reflected in the drop of the effective equation of state from $\gamma_{\text{eff}} \gtrsim 1.1$ to $\simeq 0.8$. For $\gamma_{\text{eff}} < \gamma_{\text{crit}} \simeq 1.1$, it is known that density perturbations may be amplified as the gas further contracts (Hanawa & Matsumoto 2000). The growth rate of the perturbations depends on the mode of the perturbation and the exact value of the effective equation of state. Generally, the largest modes grow most rapidly, but the achieved density contrast also depends on the initial amplitude of the perturbations. The transonic turbulence that permeates the cloud seeds the strongest perturbations on small scales, but also washes them out most quickly on these scales. In addition, the growth of small-scale perturbations below the Jeans length is suppressed by pressure gradients. The most rapidly growing perturbations therefore reside on scales just above the Jeans length.

Once the cooling time falls below the free-fall time, the sound-crossing time decreases more rapidly than the free-fall time. Perturbations can thus develop more readily and

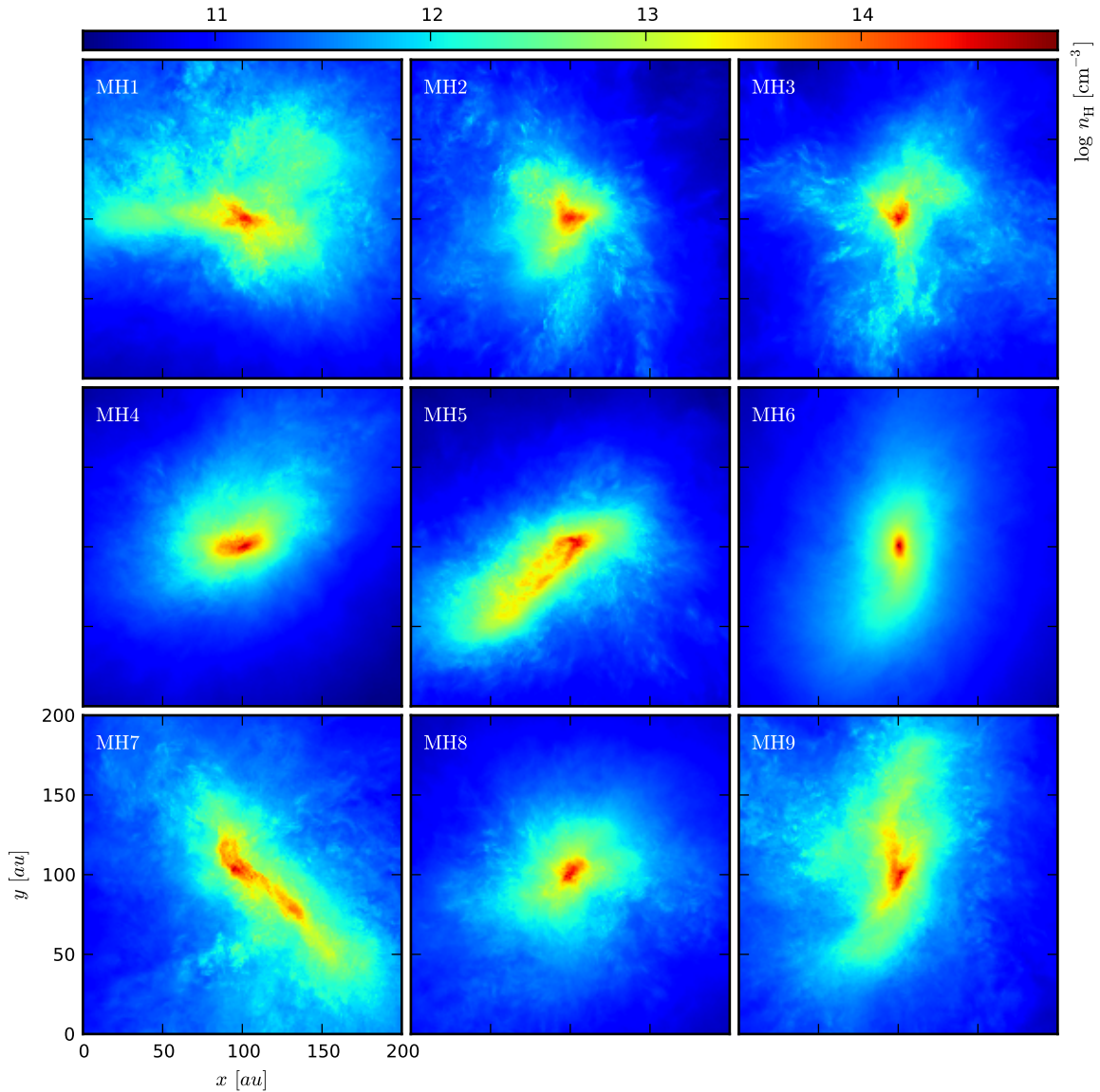


Figure 6. Number density of hydrogen nuclei in cubes of side length 200 au, centred on the densest cell in each halo. The number density is weighted with the mass and the square of the density of the cells traversed along the line of sight. Overall, the clouds are centrally concentrated, but display very irregular morphologies with filaments and knots indicative of turbulence. In MH5 and MH7, elongated clouds have formed, while in MH6 a prominent disc with little substructure is present. In MH5 and MH7, the collapse of a secondary clump has progressed far enough that it is clearly discernible from the first. Somewhat less pronounced is the sub-clump that has formed in MH1.

become apparent within the free-fall time of the primary clump. A minimum in the free-fall time over the sound-crossing time develops on scales significantly below the minimum in the cooling time over the free-fall time, since a significant change in the sound speed requires of order a cooling time, which drops to a minimum of about $t_{\text{ff}}/2$ (see Figure 2). This is reflected in the minimum of the free-fall time over the sound-crossing time being located at a few tens of au, while the minimum in the cooling time over the free-fall time is located at $\simeq 500$ au. The elevated density contrast that develops as perturbations grow is evident from the bottom right panel, which shows that the RMS density contrast

increases from about $\sigma_{\delta} \simeq 0.6$ on a scale of $\simeq 10^4$ au to well above unity on a scale of $\simeq 100$ au.

The tentative formation of a secondary clump during this stage is evident from Figure 4, which shows the number density of hydrogen nuclei, temperature, H_2 fraction, and free-fall time over sound-crossing time in the central 200 au of the box. The plane of view is perpendicular to the net angular momentum vector of the gas. A fully molecular clump with a temperature of $\simeq 700$ K has formed that is visible on the left-hand side of the panels. The potential gravitational instability of the clump is apparent from the bottom right panel, which shows that the free-fall time has dropped

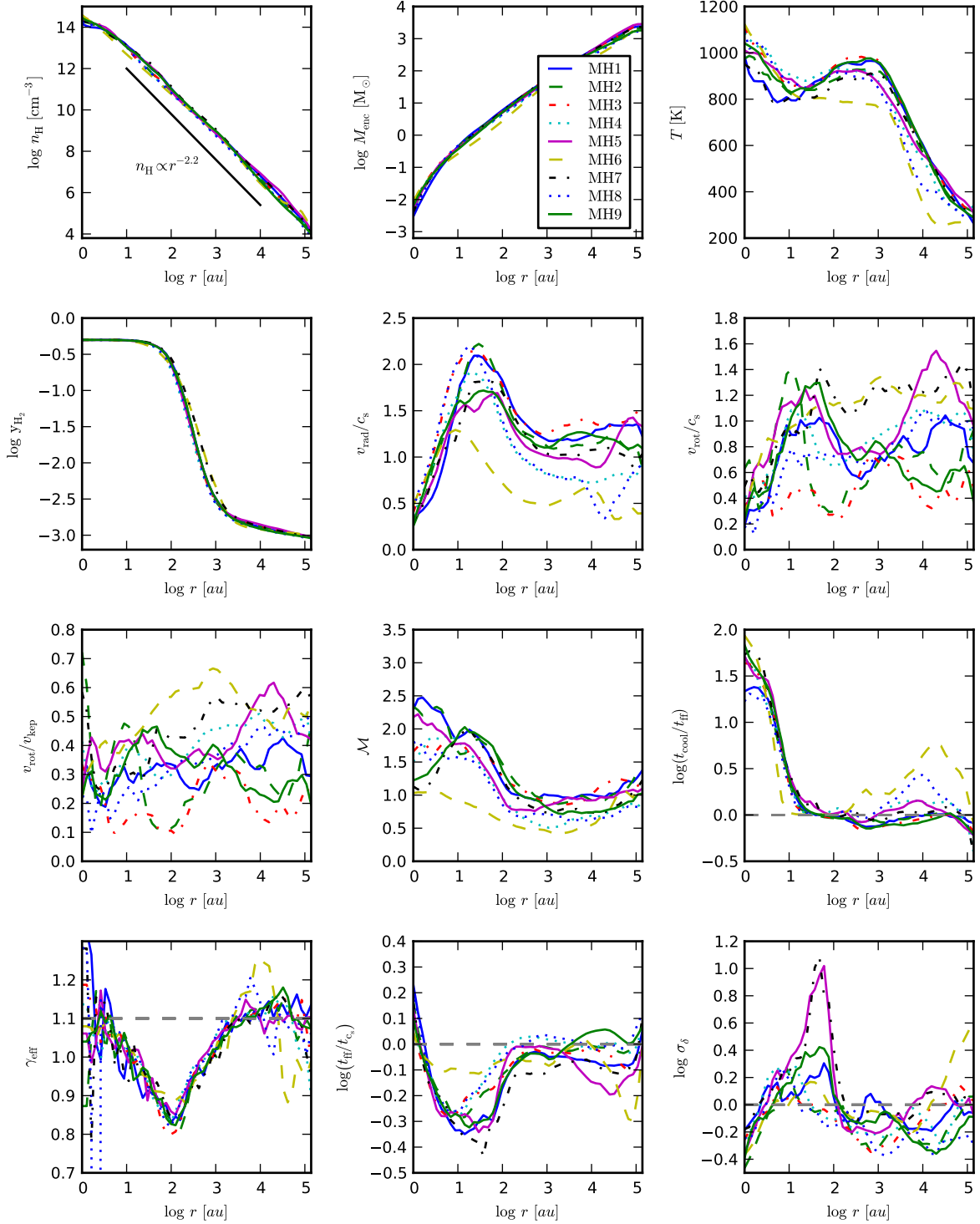


Figure 7. From top left to bottom right: number density of hydrogen nuclei, enclosed gas mass, temperature, H_2 fraction, radial velocity over sound speed, rotation velocity over sound speed, rotation velocity over Keplerian velocity, turbulent Mach number, cooling time over free-fall time, effective equation of state, free-fall time over sound-crossing time, and RMS density contrast versus radius. The solid black line in the top left panel denotes an $r^{-2.2}$ density profile. The grey dashed lines denote a cooling time equal to the free-fall time, an effective equation of state of 1.1, a free-fall time equal to the sound-crossing time, and an RMS density contrast of unity. A detailed discussion of this figure is provided in Section 3.2.

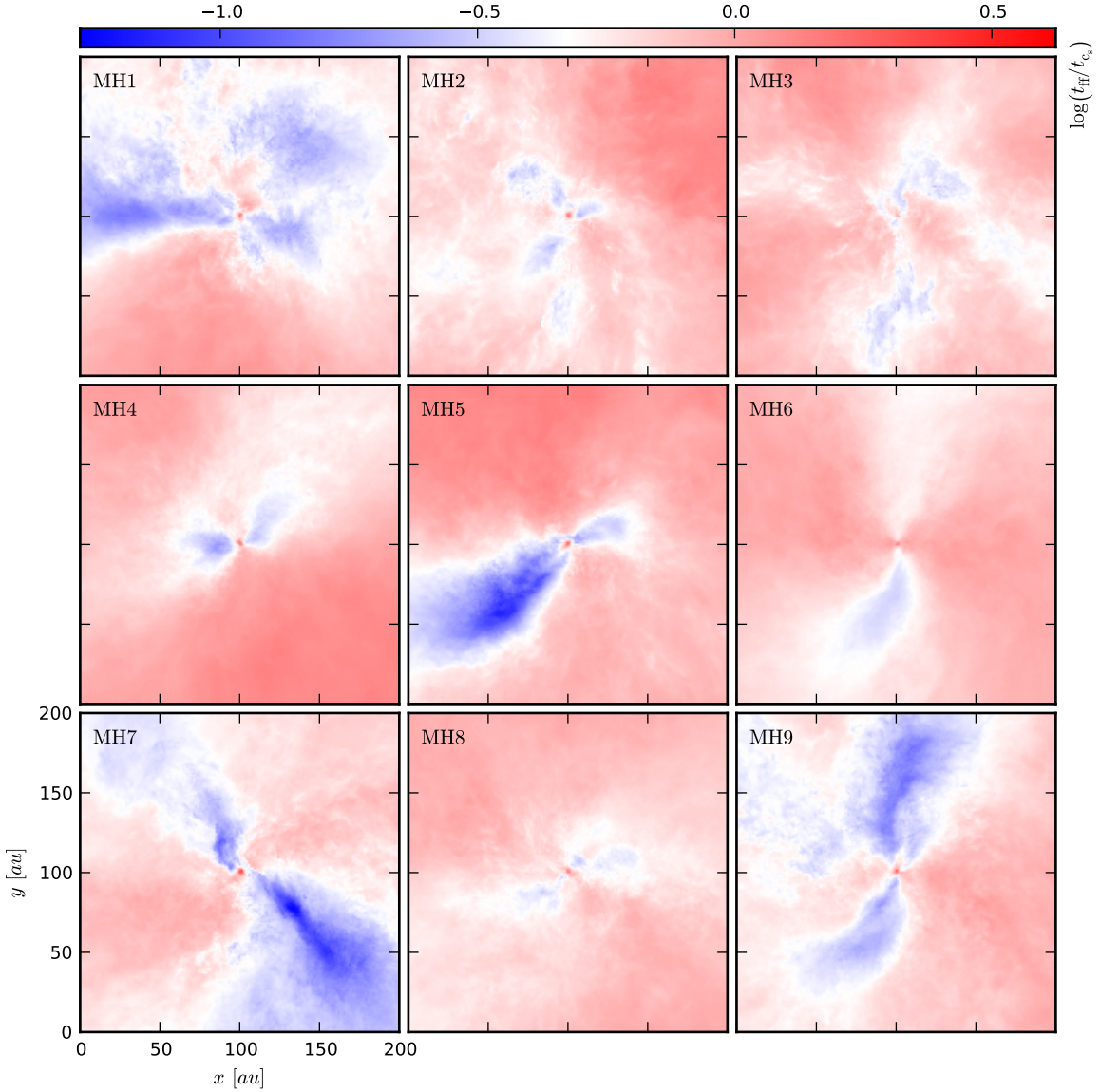


Figure 8. Free-fall time over sound-crossing time in cubes of side length 200 au, centred on the densest cell in each halo and weighted with the mass and the square of the density of the cells traversed along the line of sight. Parcels of gas that have a tendency to become Jeans-unstable are visible in MH1, MH5, MH7 and MH9. A comparison with Figure 6 reveals that they are correlated with the isolated, dense clumps visible in this figure.

to well below the sound-crossing time. In Section 3.3, we investigate whether this clump has acquired enough mass to become Jeans-unstable in its own right, and whether it collapses before it is accreted by the primary clump.

The growth of perturbations enabled by the chemothermal instability is further evident from Figure 5, which shows the temperature, escape fraction, cooling time over free-fall time, and free-fall time over sound-crossing time versus number density of hydrogen nuclei. The logarithm of the mass per bin over the total mass in the box is color-coded from blue (lowest) to red (highest), and the solid lines show the mass-weighted average value versus density. Above a density of $n_{\text{H}} \simeq 10^{10} \text{ cm}^{-3}$, the temperature distribution widens and some parcels of gas cool to as low as $\simeq 200 \text{ K}$,

while others are heated to over 2000 K. The photon escape fraction at a given density fluctuates by up to two orders of magnitude, such that some regions of the cloud cool very efficiently and may become Jeans-unstable. This is reflected by the substantial amounts of gas with a free-fall time below the sound-crossing time. Another noteworthy feature is the shock-heating of a parcel of gas to over 3000 K, which is apparent from the peak in temperature between $n_{\text{H}} \simeq 10^8$ and $\simeq 10^{10} \text{ cm}^{-3}$. The elevated temperature results in collisional dissociation of H_2 down to a level of $y_{\text{H}_2} \simeq 10^{-6}$. Similar shock-heated parcels of gas were also found in Turk et al. (2010).

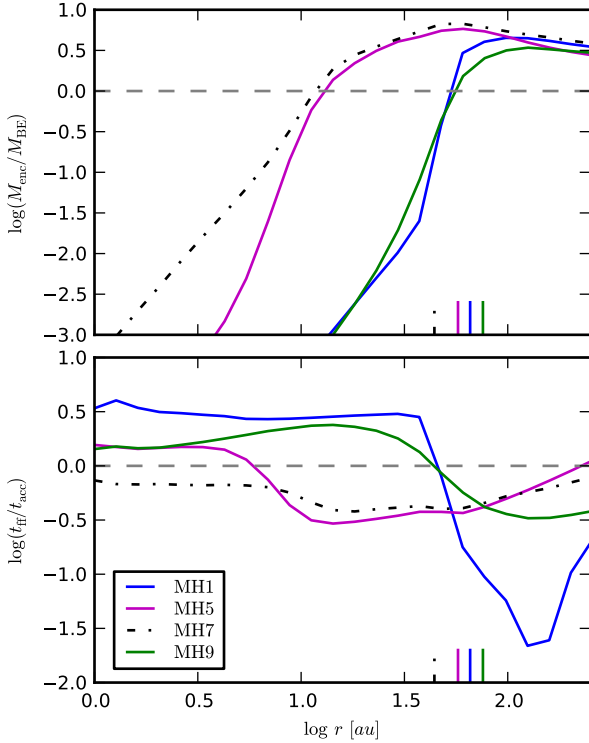


Figure 9. Enclosed mass over Bonnor-Ebert mass (top panel), and free-fall time over accretion time (bottom panel) versus radius centred on the secondary clumps that have formed in MH1, MH5, MH7 and MH9. The vertical lines denote the separation of the clumps from the center of the cloud. Only MH5 and MH7 are likely to fragment during the initial free-fall phase, since the radius at which the enclosed mass exceeds the Bonnor-Ebert mass and the free-fall time drops to below the sound-crossing is significantly smaller than the separation of the clumps from the center of the cloud. This is not the case in MH1 and MH9, where the primary and secondary clumps are nearly indistinguishable.

3.2 Halo sample

In Figure 6, we show the number density of hydrogen nuclei in a face-on views of the central 200 au in the various haloes investigated. Most clouds display a centrally concentrated, irregular morphology with a multitude of filaments and knots, while MH4 and MH6 have a more regular morphology and less substructure. In MH5 and MH7, an elongated cloud has formed, while in MH6 a prominent disc with little substructure is present. In MH5 and MH7, the collapse of a secondary clump has progressed far enough that it is clearly discernible from the first. Somewhat less pronounced is the sub-clump that has formed in MH1.

Figure 7 shows radially averaged profiles of various physical quantities. From top left to bottom right, the panels show the number density of hydrogen nuclei, enclosed gas mass, temperature, H_2 fraction, radial velocity over sound speed, rotation velocity over sound speed, rotation velocity over Keplerian velocity, turbulent Mach number, cooling time over free-fall time, effective equation of state, free-fall time over sound-crossing time, and RMS density contrast versus radius. The rotation velocity vector \mathbf{v}_{rot} is given by the sum of the angular momenta of the contributing cells

divided by the total mass M_{tot} and radius of the bin. The Keplerian velocity is given by $v_{\text{kep}} = \sqrt{GM_{\text{enc}}/r}$, where M_{enc} is the enclosed mass. The turbulent velocity is given by

$$v_{\text{turb}} = \frac{\sqrt{\sum_i m_i (\mathbf{v}_i - \mathbf{v}_{\text{rad}} - \mathbf{v}_{\text{rot}})^2}}{M_{\text{tot}}}, \quad (11)$$

where \mathbf{v}_i is the velocity vector of a cell, and \mathbf{v}_{rad} the radial velocity vector of the bin. The turbulent Mach number \mathcal{M} is given by $\mathcal{M} = v_{\text{turb}}/c_s$, where c_s is the sound speed.

The top left panel in Figure 7 shows that the gas clouds have an approximate $r^{-2.2}$ profile, which is expected for $\gamma_{\text{eff}} \simeq 1.1$ (Larson 1969). In MH5 and MH7, bumps in the density profile at a distance of a few tens of au from the center indicate that secondary clumps have begun to form. The enclosed mass is less sensitive to fluctuations in the density and does not show any prominent features. The temperature rises to about 1000 K on a scale of $\simeq 1000$ au, followed by a slight drop to 800 K on a scale of 10 au, and an increase to over 1000 K on scales below $\simeq 1$ au. In MH6, HD cooling becomes important and prolongs the initial cooling phase to $n_H \simeq 10^6 \text{ cm}^{-3}$, after which the temperature increases more sharply compared to haloes in which HD cooling does not become important. This leads to a slower collapse of the cloud during which turbulent motions decay and a pronounced disc forms (Clark et al. 2011). The molecular hydrogen fraction shows little scatter among the individual haloes and increases from $y_{H_2} \simeq 10^{-3}$ at $\simeq 1000$ au to fully molecular with $y_{H_2} \simeq 0.5$ at a few tens of au. The radial velocity peaks on a scale of a few tens of au as the gas cools slightly and loses some pressure support.

All clouds are substantially rotationally supported. The average rotation velocity is of order the sound speed and comparable to the radial velocity. Most haloes display a peak in the respective ratio on a scale of a few tens of au, which is however not present in the profiles showing the rotation velocity over the Keplerian velocity. In MH6, the cooling time briefly increases to nearly an order of magnitude above the free-fall time, and the prominent disc visible in Figure 6 forms. This is reflected by an increase of the rotation velocity over the Keplerian velocity to $\simeq 0.6$ on a scale of $\simeq 1000$ au. The respective value fluctuates by about a factor of two in the course of the collapse of a cloud, and the mean among the haloes is $\simeq 1/3$. The turbulent Mach number is generally close to unity, implying that the clouds are in nearly equal parts supported by thermal pressure, rotation and turbulence. Below $\simeq 100$ au, the temperature drops slightly and the turbulence transitions into the supersonic regime with $\mathcal{M} \simeq 2$. The turbulent support is also apparent from the filamentary appearance of the gas shown in Figure 6.

Following the rapid increase of the H_2 fraction on a scale of $\simeq 1000$ au, the cooling rate increases and the cooling time drops slightly below the free-fall time. The effective equation of state of the gas decreases from $\gamma_{\text{eff}} \simeq 1.1$ to $\simeq 0.8$ on a scale of $\simeq 100$ au, and the free-fall time drops below the sound-crossing time, with MH1, MH5, MH7 and MH9 showing the most pronounced dip. During this phase, density perturbations seeded by the slightly supersonic turbulence grow more rapidly, and in these haloes the RMS density contrast increases to well above unity. In MH5 and MH7, the density contrast even increases by an order of magnitude.

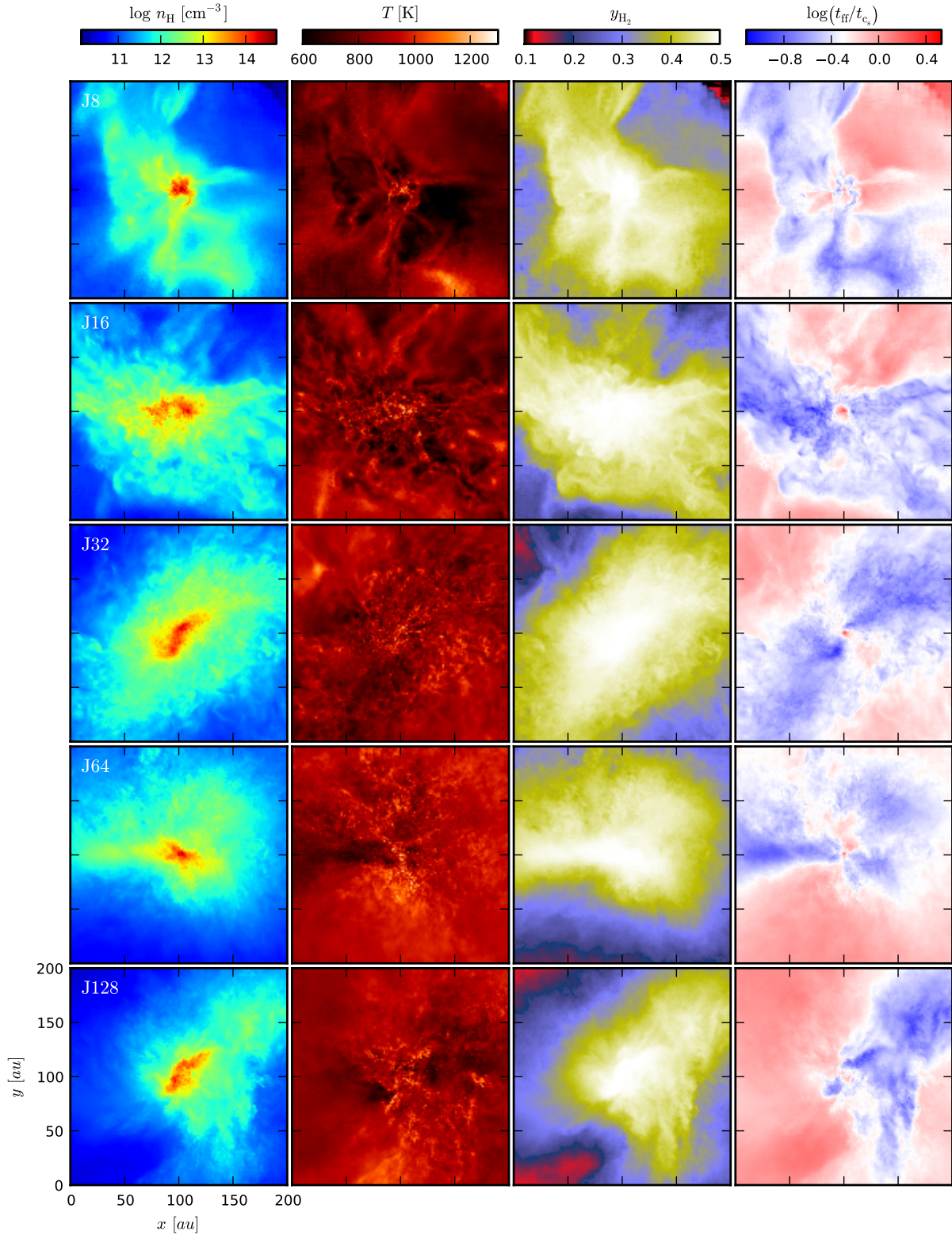


Figure 10. From left to right: number density of hydrogen nuclei, temperature, H_2 fraction, and free-fall time over sound-crossing time in cubes of side length 200 au, centred on the densest cell in the halo and weighted with the mass and the square of the density of the cells traversed along the line of sight. From top to bottom: simulations employing 8, 16, 32, 64, and 128 cells per Jeans length according to Turk et al. (2010) in MH1. Except for an increasing amount of small-scale structure, there is no apparent trend in any of the shown quantities as the resolution is increased.

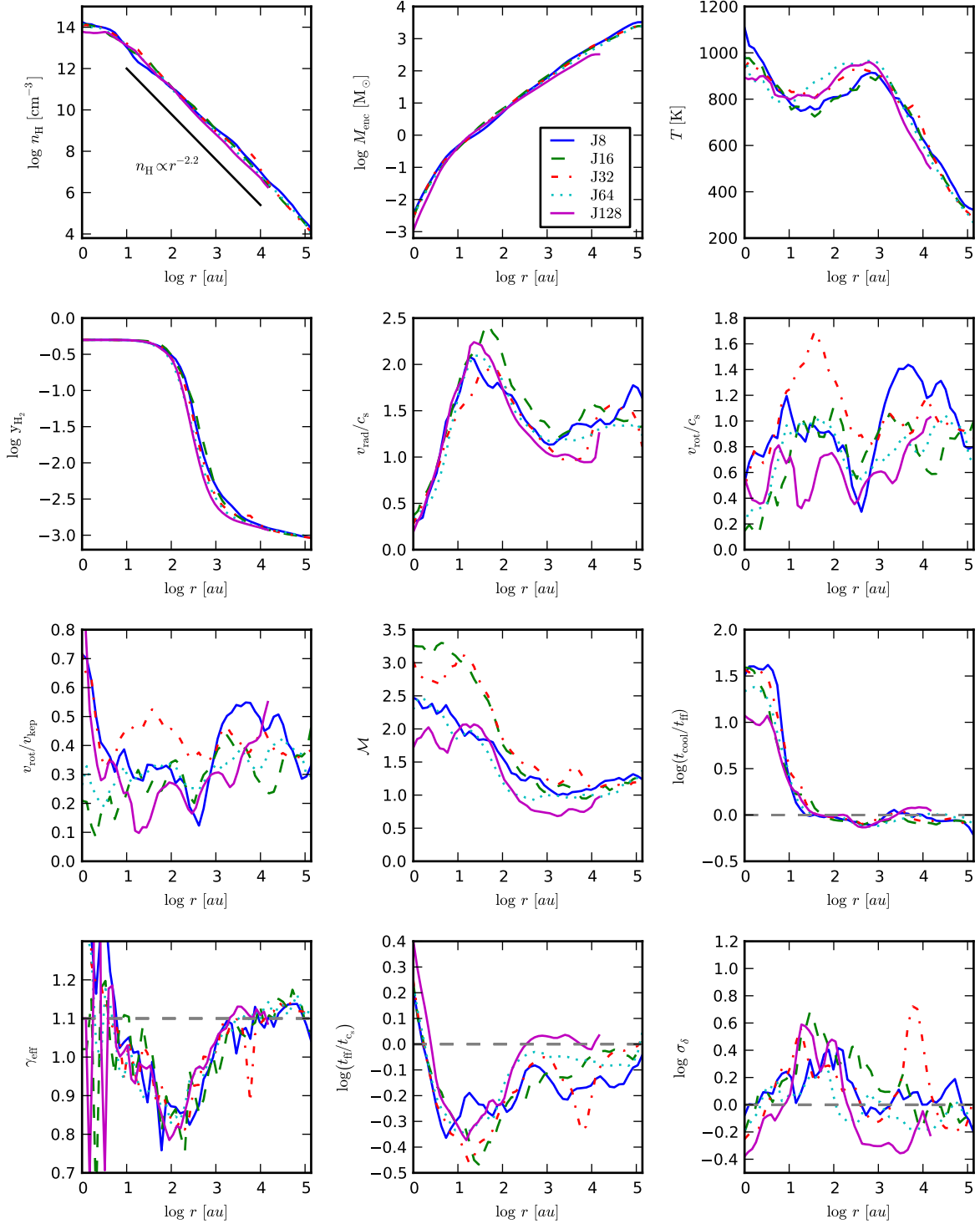


Figure 11. From top left to bottom right: number density of hydrogen nuclei, enclosed gas mass, temperature, H_2 fraction, radial velocity over sound speed, rotation velocity over sound speed, rotation velocity over Keplerian velocity, turbulent Mach number, cooling time over free-fall time, effective equation of state, free-fall time over sound-crossing time, and RMS density contrast versus radius for 8, 16, 32, 64, and 128 cells per Jeans length according to Turk et al. (2010) in MH1. The solid black line in the top left panel denotes an $r^{-2.2}$ density profile. The grey dashed lines denote a cooling time equal to the free-fall time, an effective equation of state of 1.1, a free-fall time equal to the sound-crossing time, and an RMS density contrast of unity. Qualitatively, the profiles are similar among the various simulations, but also display a substantial amount of scatter. We find no clear trend in any of the profiles as the resolution is increased.

The formation of secondary clumps in these haloes is evident from Figure 8, which shows the free-fall time over the sound-crossing time in the central 200 au of the box. Parcels of gas with a tendency to become gravitationally unstable are apparent. A comparison with Figure 6 shows that these regions are highly correlated with the isolated, dense clumps visible in this figure.

Based on Figure 9, we investigate whether the clumps in MH1, MH5, MH7 and MH9 have accumulated enough mass to become gravitationally unstable, and whether they will collapse before they are accreted by the primary clump. To this end, the top panel shows the enclosed mass over the locally estimated Bonnor-Ebert mass (Ebert 1955; Bonnor 1956), centred on the minimum in the free-fall time over the sound-crossing time as identified in Figure 8. The Bonnor-Ebert mass is computed as the mass-weighted average among the cells within a given radius according to:

$$M_{\text{BE}} \simeq 15 M_{\odot} \left(\frac{n_{\text{H}}}{\text{cm}^{-3}} \right)^{-1/2} \left(\frac{T}{\text{K}} \right)^{3/2} \mu^{-3/2} \gamma^2. \quad (12)$$

The bottom panel shows the free-fall time over the accretion time. The free-fall time is computed by using the mass enclosed within a given radius, and the accretion time by $t_{\text{acc}} = d/v_{\text{rad}}$, where d denotes the distance of the clump from the center of the cloud (vertical lines in Figure 9), and v_{rad} the net radial velocity of the mass enclosed within a given radius with respect to the center of the cloud.

From this figure, it is evident that only the clouds in MH5 and MH7 are likely to fragment during the initial free-fall phase. The enclosed mass exceeds the Bonnor-Ebert mass at small enough radii that the clumps are Jeans-unstable in their own right, which is not the case in MH1 and MH9, where there is no clear distinction between the primary and secondary clumps. Furthermore, since the free-fall time falls below the accretion time at radii significantly smaller than the separation of the clumps from the center of the cloud, the clouds in MH5 and MH7 will likely collapse before they are accreted. However, the separation of the clumps is only of order a few tens of au – in contrast to the 800 au that were found in Turk et al. (2009). Based on the results of Greif et al. (2012), it thus appears likely that the secondary clumps will merge well before radiation feedback can evacuate enough mass to alleviate the strong gravitational torques that are present in the disc. On the other hand, the secondary clump found in Turk et al. (2012) has a much higher chance of surviving and forming a separate Population III star.

3.3 Resolution study

Previous studies of Population III star formation have argued that the nature of primordial gas clouds depends sensitively on the employed resolution (e.g. Turk et al. 2012). We investigate whether the resolution requirements found in these simulations also apply to the moving-mesh simulations presented here. To this end, we employ between 8 and 128 cells per Jeans length according to Turk et al. (2010), using the halo that was described in detail in Section 3.1 (MH1).

In Figure 10, we show the number density of hydrogen nuclei, temperature, H_2 fraction, and free-fall time over sound-crossing time in the central 200 au of the box. The morphology of the gas is highly irregular in all simulations,

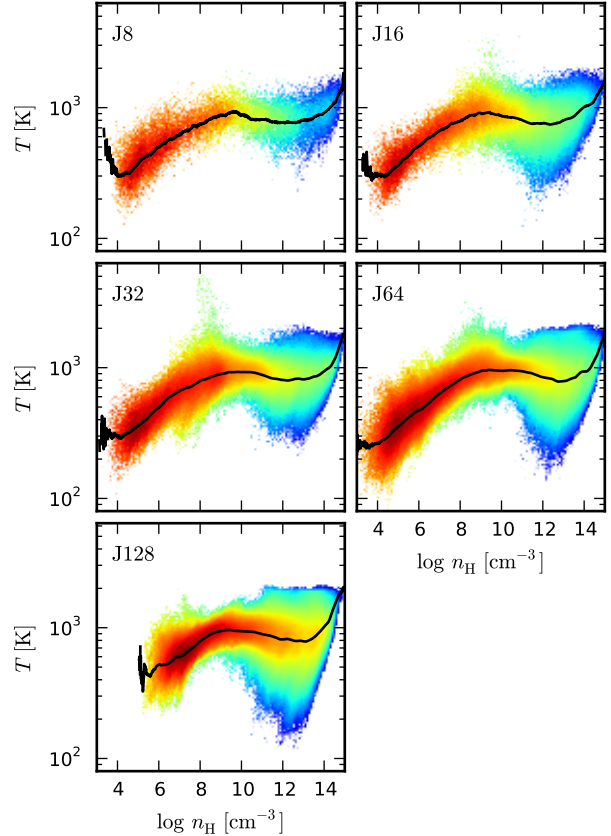


Figure 12. Temperature versus number density of hydrogen nuclei for 8, 16, 32, 64, and 128 cells per Jeans length according to Turk et al. (2010) in MH1. The logarithm of the mass per bin over the total mass in the box is color-coded from blue (lowest) to red (highest), and the solid lines show the mass-weighted average value versus density. As the resolution is increased, the dispersion of the gas increases in particular in phases in which the gas cools efficiently, which is most likely due to the better sampling of the extreme ends of the distribution.

and the amount of small-scale structure increases as the resolution is increased. However, we do not find any other convincing trend in the density, temperature, H_2 fraction, and free-fall time over sound-crossing time. Regions with a tendency to become gravitationally unstable are visible in all simulations, but their size or abundance does not decrease or increase as the resolution is increased.

In Figure 11, we show radial profiles of the physical quantities discussed in Section 3.2. In the J128 case, an additional resimulation was necessary to increase the dynamic range of the simulation, such that only the central $\simeq 10^4$ au are shown. Qualitatively, the profiles agree well with each other, but there is also a substantial amount of scatter. As in Figure 10, we find no clear trend in any of the shown physical quantities as the resolution is increased. In Figure 12, we show the distribution of the gas in density and temperature. For increasing resolution, the temperature dispersion increases when the gas cools efficiently. This is most likely due to the better sampling of the extreme ends of the distribution, and may raise the probability for finding gravitationally unstable clumps of gas. However, we find no clear evidence for such a trend from Figures 10 and 11. Instead,

the random nature of self-gravitating collapse and the non-linear rate equations that govern the chemical and thermal evolution of the cloud appear to dominate over all other trends that may be present. In particular, the differences between simulations with different resolution are similar to the differences between simulations of different haloes.

4 SUMMARY AND CONCLUSIONS

We have investigated the operation of the chemo-thermal instability in primordial, star-forming clouds with a suite of nine high-resolution simulations. At densities $n_{\text{H}} \gtrsim 10^8 \text{ cm}^{-3}$, three-body reactions rapidly increase the H_2 fraction and trigger potential runaway cooling, which is counteracted by the chemical heating of the gas due to the release of the binding energy of the H_2 molecule, and the increasing optical depth to H_2 line emission. The competition between these processes results in a drop of the cooling time below the free-fall time on a scale of $\simeq 1000 \text{ au}$, such that the effective equation of state of the gas decreases from $\gamma_{\text{eff}} \simeq 1.1$ to $\simeq 0.8$. As a result, the free-fall time drops to well below the sound-crossing time on scales $\lesssim 100 \text{ au}$, and perturbations seeded by the transonic turbulence within the cloud may grow large enough that they trigger the gravitational collapse of secondary clumps. In two of the nine haloes investigated, enough mass accumulates in the secondary clumps that they will most likely collapse before they are accreted by the primary clump.

In addition to the main simulation suite, we have performed a resolution study to investigate how our results depend on the number of cells employed per Jeans length. Apart from a broader temperature distribution of the gas, we find no convincing trend in the appearance of the cloud or other physical quantities as the resolution is increased. Instead, the turbulent nature of self-gravitating collapse and the non-linear rate equations that govern the chemical and thermal evolution of the cloud appear to dominate over all other trends. The differences between simulations with different resolution are comparable to the differences between simulations of different haloes.

Qualitatively, our results agree well with previous three-dimensional simulations, but we also find a few differences. In the simulations of Yoshida et al. (2006), the primordial gas cloud remained marginally stable at high densities. Most haloes in our study follow this trend, but in some cases the transonic turbulence present in the gas seeds large enough perturbations that fragmentation may occur. Compared to Turk et al. (2009), we find very good agreement concerning the relative fraction of haloes in which fragmentation occurs: in the present study, the gas fragments in two out of nine haloes, while in Turk et al. (2009) one out of five haloes fragments. However, this result may be somewhat misleading, since fragmentation in our simulations occurs on a scale of a few tens of au, while in Turk et al. (2009) the secondary clump forms on a scale of $\simeq 1000 \text{ au}$.

Apart from systematic differences concerning the gravitational and hydrodynamic solvers, an additional source of discrepancy with respect to Turk et al. (2009) is the chemical model employed. The most important differences are the choice of the H_2 cooling function, the three-body formation rate, and a direction-dependent escape fraction for H_2

line emission, which raises the cooling efficiency of the gas (Turk et al. 2011). As a result, the temperature of the gas at $\simeq 1 \text{ au}$ from the center in our study is around 1000 K , while in Turk et al. (2009) it exceeds 2000 K . Collisional dissociation becomes effective before collision-induced emission cools the gas, and as a result the H_2 fraction in Turk et al. (2009) has begun to decrease at radii where we find that the gas is still fully molecular. Finally, Turk et al. (2012) found that the gas becomes more rotationally supported when less than 32 cells per Jeans length are used. We do not find such a trend even when the resolution is decreased to only eight cells per Jeans length, which is close to the bare minimum required to resolve self-gravitating collapse (Truelove et al. 1998; Greif et al. 2011). At high resolution, both methods yield very similar cloud morphologies.

One of the caveats of this study is that we have not taken supersonic streaming motions into account, which affects the mass scale and virialisation process of the haloes in which Population III star formation occurs (Tselikhovich & Hirata 2010; Greif et al. 2011; Maio et al. 2011; Stacy et al. 2011; Naoz et al. 2012, 2013; O’Leary & McQuinn 2012). We also neglect the potential heating of the gas by self-annihilating DM (Freese et al. 2008; Iocco et al. 2008; Ripamonti et al. 2010; Smith et al. 2012). Instead of performing full radiation transfer for H_2 line emission, we resort to approximate, on-the-spot methods that likely reduce the cooling efficiency of the gas. Furthermore, some of the employed chemical rate equations are highly uncertain (Glover & Abel 2008; Turk et al. 2011). We also neglect the influence of magnetic fields, which might become dynamically important during the initial collapse (Machida et al. 2008; Xu et al. 2008; Schleicher et al. 2009, 2010; Sur et al. 2010; Federrath et al. 2011; Schober et al. 2012; Turk et al. 2012).

In concluding, we note that while only a fraction of the star-forming clouds in minihaloes are expected to fragment during their initial collapse, this by no means precludes fragmentation at a later stage, when the gas becomes rotationally supported in a Keplerian disc, and the infall rate is significantly reduced compared to simple one-dimensional estimates (Greif et al. 2012). The chemo-thermal instability and the resulting gravitational instability may therefore have substantially more time to develop than is apparent from the limited period of time simulated here.

ACKNOWLEDGEMENTS

THG would like to thank Tom Abel and Naoki Yoshida for stimulating discussions that helped improve this work. The simulations were carried out at the Rechenzentrum Garching (RZG) and the Texas Advanced Computing Center (TACC) under XSEDE allocation AST130020 (for THG) and project A-astro (for VB). VB acknowledges support from NSF through grant AST-1009928.

REFERENCES

- Abel T., Anninos P., Norman M. L., Zhang Y., 1998, *ApJ*, 508, 518
- Abel T., Anninos P., Zhang Y., Norman M. L., 1997, *New Astronomy*, 2, 181

- Abel T., Bryan G. L., Norman M. L., 2000, *ApJ*, 540, 39
- Abel T., Bryan G. L., Norman M. L., 2002, *Science*, 295, 93
- Abel T., Wise J. H., Bryan G. L., 2007, *ApJ*, 659, L87
- Alvarez M. A., Bromm V., Shapiro P. R., 2006, *ApJ*, 639, 621
- Barkana R., Loeb A., 2001, *Phys. Rep.*, 349, 125
- Bate M. R., Bonnell I. A., Price N. M., 1995, *MNRAS*, 277, 362
- Bonnor W. B., 1956, *MNRAS*, 116, 351
- Bromm V., Coppi P. S., Larson R. B., 1999, *ApJ*, 527, L5
- Bromm V., Coppi P. S., Larson R. B., 2002, *ApJ*, 564, 23
- Bromm V., Kudritzki R. P., Loeb A., 2001, *ApJ*, 552, 464
- Bromm V., Larson R. B., 2004, *ARA&A*, 42, 79
- Bromm V., Loeb A., 2004, *New Astronomy*, 9, 353
- Carlberg R. G., 1981, *MNRAS*, 197, 1021
- Carr B. J., Bond J. R., Arnett W. D., 1984, *ApJ*, 277, 445
- Ciardi B., Ferrara A., 2005, *Space Science Reviews*, 116, 625
- Clark P. C., Glover S. C. O., Klessen R. S., 2008, *ApJ*, 672, 757
- Clark P. C., Glover S. C. O., Klessen R. S., Bromm V., 2011, *ApJ*, 727, 110
- Clark P. C., Glover S. C. O., Smith R. J., Greif T. H., Klessen R. S., Bromm V., 2011, *Science*, 331, 1040
- Couchman H. M. P., Rees M. J., 1986, *MNRAS*, 221, 53
- Dijkstra M., Haiman Z., Rees M. J., Weinberg D. H., 2004, *ApJ*, 601, 666
- Ebert R., 1955, *Z. Astrophys.*, 37, 217
- Federrath C., Banerjee R., Clark P. C., Klessen R. S., 2010, *ApJ*, 713, 269
- Federrath C., Sur S., Schleicher D. R. G., Banerjee R., Klessen R. S., 2011, *ApJ*, 731, 62
- Flower D. R., Le Bourlot J., Pineau des Forêts G., Roueff E., 2000, *MNRAS*, 314, 753
- Freese K., Bodenheimer P., Spolyar D., Gondolo P., 2008, *ApJ*, 685, L101
- Galli D., Palla F., 1998, *A&A*, 335, 403
- Glover S., 2005, *Space Science Reviews*, 117, 445
- Glover S., 2013, in Wiklind T., Mobasher B., Bromm V., eds, *Astrophysics and Space Science Library Vol. 396 of Astrophysics and Space Science Library, The First Stars*. p. 103
- Glover S. C. O., Abel T., 2008, *MNRAS*, 388, 1627
- Glover S. C. O., Jappsen A.-K., 2007, *ApJ*, 666, 1
- Greif T. H., Bromm V., Clark P. C., Glover S. C. O., Smith R. J., Klessen R. S., Yoshida N., Springel V., 2012, *MNRAS*, 424, 399
- Greif T. H., Glover S. C. O., Bromm V., Klessen R. S., 2010, *ApJ*, 716, 510
- Greif T. H., Johnson J. L., Klessen R. S., Bromm V., 2009, *MNRAS*, 399, 639
- Greif T. H., Springel V., White S. D. M., Glover S. C. O., Clark P. C., Smith R. J., Klessen R. S., Bromm V., 2011, *ApJ*, 737, 75
- Greif T. H., White S. D. M., Klessen R. S., Springel V., 2011, *ApJ*, 736, 147
- Haiman Z., Thoul A. A., Loeb A., 1996, *ApJ*, 464, 523
- Hanawa T., Matsumoto T., 2000, *PASJ*, 52, 241
- Heger A., Fryer C. L., Woosley S. E., Langer N., Hartmann D. H., 2003, *ApJ*, 591, 288
- Hindmarsh A. C., Brown P. N., Grant K. E., Lee S. L., Serban R., Shumaker D. E., Woodward C. S., 2005, *ACM Transactions on Mathematical Software*, 31, 363
- Hirano S., Umeda H., Yoshida N., 2011, *ApJ*, 736, 58
- Hirasawa T., 1969, *Progress of Theoretical Physics*, 42, 523
- Hosokawa T., Omukai K., Yoshida N., Yorke H. W., 2011, *Science*, 334, 1250
- Hutchins J. B., 1976, *ApJ*, 205, 103
- Iocco F., Bressan A., Ripamonti E., Schneider R., Ferrara A., Marigo P., 2008, *MNRAS*, 390, 1655
- Jappsen A.-K., Klessen R. S., Larson R. B., Li Y., Mac Low M.-M., 2005, *A&A*, 435, 611
- Johnson J. L., Bromm V., 2006, *MNRAS*, 366, 247
- Johnson J. L., Greif T. H., Bromm V., 2007, *ApJ*, 665, 85
- Kashlinsky A., Rees M. J., 1983, *MNRAS*, 205, 955
- Komatsu E., et al., 2009, *ApJS*, 180, 330
- Krumholz M. R., McKee C. F., Klein R. I., 2004, *ApJ*, 611, 399
- Larson R. B., 1969, *MNRAS*, 145, 271
- Le Bourlot J., Pineau des Forêts G., Flower D. R., 1999, *MNRAS*, 305, 802
- Lipovka A., Núñez-López R., Avila-Reese V., 2005, *MNRAS*, 361, 850
- Loeb A., 2010, *How Did the First Stars and Galaxies Form?*
- Mac Low M.-M., Ferrara A., 1999, *ApJ*, 513, 142
- Machida M. N., Matsumoto T., Inutsuka S.-i., 2008, *ApJ*, 685, 690
- Madau P., Ferrara A., Rees M. J., 2001, *ApJ*, 555, 92
- Maio U., Koopmans L. V. E., Ciardi B., 2011, *MNRAS*, 412, L40
- Matsuda T., Satō H., Takeda H., 1969, *Progress of Theoretical Physics*, 42, 219
- McGreer I. D., Bryan G. L., 2008, *ApJ*, 685, 8
- McKee C. F., Tan J. C., 2008, *ApJ*, 681, 771
- Nakamura F., Umemura M., 1999, *ApJ*, 515, 239
- Nakamura F., Umemura M., 2002, *ApJ*, 569, 549
- Naoz S., Yoshida N., Gnedin N. Y., 2012, *ApJ*, 747, 128
- Naoz S., Yoshida N., Gnedin N. Y., 2013, *ApJ*, 763, 27
- Oh S. P., Haiman Z., 2002, *ApJ*, 569, 558
- O’Leary R. M., McQuinn M., 2012, *ApJ*, 760, 4
- Omukai K., Nishi R., 1998, *ApJ*, 508, 141
- Omukai K., Yoshii Y., 2003, *ApJ*, 599, 746
- Palla F., Salpeter E. E., Stahler S. W., 1983, *ApJ*, 271, 632
- Peebles P. J. E., Dicke R. H., 1968, *ApJ*, 154, 891
- Read J. I., Pontzen A. P., Viel M., 2006, *MNRAS*, 371, 885
- Ricotti M., Gnedin N. Y., Shull J. M., 2002, *ApJ*, 575, 33
- Ripamonti E., 2007, *MNRAS*, 376, 709
- Ripamonti E., Abel T., 2004, *MNRAS*, 348, 1019
- Ripamonti E., Iocco F., Ferrara A., Schneider R., Bressan A., Marigo P., 2010, *MNRAS*, 406, 2605
- Sabano Y., Yoshii Y., 1977, *PASJ*, 29, 207
- Saslaw W. C., Zipoy D., 1967, *Nature*, 216, 976
- Schaerer D., 2002, *A&A*, 382, 28
- Schleicher D. R. G., Banerjee R., Sur S., Arshakian T. G., Klessen R. S., Beck R., Spaans M., 2010, *A&A*, 522, A115
- Schleicher D. R. G., Galli D., Glover S. C. O., Banerjee R., Palla F., Schneider R., Klessen R. S., 2009, *ApJ*, 703, 1096
- Schober J., Schleicher D., Federrath C., Klessen R., Banerjee R., 2012, *Phys. Rev. E*, 85, 026303
- Silk J., 1977, *ApJ*, 211, 638
- Silk J., 1983, *MNRAS*, 205, 705

- Smith R. J., Iocco F., Glover S. C. O., Schleicher D. R. G., Klessen R. S., Hirano S., Yoshida N., 2012, *ApJ*, 761, 154
- Springel V., 2010, *MNRAS*, 401, 791
- Springel V., White S. D. M., Tormen G., Kauffmann G., 2001, *MNRAS*, 328, 726
- Stacy A., Bromm V., Loeb A., 2011, *ApJ*, 730, L1
- Stacy A., Greif T. H., Bromm V., 2010, *MNRAS*, 403, 45
- Stacy A., Greif T. H., Bromm V., 2012, *MNRAS*, 422, 290
- Stancil P. C., Lepp S., Dalgarno A., 1998, *ApJ*, 509, 1
- Sur S., Schleicher D. R. G., Banerjee R., Federrath C., Klessen R. S., 2010, *ApJ*, 721, L134
- Takeda H., Satō H., Matsuda T., 1969, *Progress of Theoretical Physics*, 41, 840
- Tan J. C., McKee C. F., 2004, *ApJ*, 603, 383
- Tegmark M., Silk J., Rees M. J., Blanchard A., Abel T., Palla F., 1997, *ApJ*, 474, 1
- Thoul A. A., Weinberg D. H., 1996, *ApJ*, 465, 608
- Truelove J. K., Klein R. I., McKee C. F., Holliman II J. H., Howell L. H., Greenough J. A., Woods D. T., 1998, *ApJ*, 495, 821
- Tseliaikhovich D., Hirata C., 2010, *Phys. Rev. D*, 82, 083520
- Turk M. J., Abel T., O'Shea B., 2009, *Science*, 325, 601
- Turk M. J., Clark P., Glover S. C. O., Greif T. H., Abel T., Klessen R., Bromm V., 2011, *ApJ*, 726, 55
- Turk M. J., Norman M. L., Abel T., 2010, *ApJ*, 725, L140
- Turk M. J., Oishi J. S., Abel T., Bryan G. L., 2012, *ApJ*, 745, 154
- Uehara H., Susa H., Nishi R., Yamada M., Nakamura T., 1996, *ApJ*, 473, L95
- Umeda H., Nomoto K., 2003, *Nature*, 422, 871
- Vorobyov E. I., DeSouza A. L., Basu S., 2013, *ApJ*, 768, 131
- Wada K., Venkatesan A., 2003, *ApJ*, 591, 38
- Whalen D., O'Shea B. W., Smidt J., Norman M. L., 2008, *ApJ*, 679, 925
- Wise J. H., Abel T., 2008, *ApJ*, 685, 40
- Wrathmall S. A., Flower D. R., 2007, *Journal of Physics B Atomic Molecular Physics*, 40, 3221
- Xu H., O'Shea B. W., Collins D. C., Norman M. L., Li H., Li S., 2008, *ApJ*, 688, L57
- Yoneyama T., 1972, *PASJ*, 24, 87
- Yoon S.-C., Iocco F., Akiyama S., 2008, *ApJ*, 688, L1
- Yoshida N., Oh S. P., Kitayama T., Hernquist L., 2007, *ApJ*, 663, 687
- Yoshida N., Omukai K., Hernquist L., 2008, *Science*, 321, 669
- Yoshida N., Omukai K., Hernquist L., Abel T., 2006, *ApJ*, 652, 6